High-speed x-ray phase contrast imaging and digital image correlation analysis of microscale shock response of an additively manufactured energetic material simulant

Cite as: J. Appl. Phys. **127**, 235902 (2020); https://doi.org/10.1063/5.0003525
Submitted: 02 February 2020 • Accepted: 30 May 2020 • Published Online: 15 June 2020

Karla B. Wagner, Amirreza Keyhani, Andrew K. Boddorff, et al.

Journal of Applied Physics ARTICLE scitation.org/journal/jap

High-speed x-ray phase contrast imaging and digital image correlation analysis of microscale shock response of an additively manufactured energetic material simulant

Cite as: J. Appl. Phys. **127**, 235902 (2020); doi: 10.1063/5.0003525
Submitted: 2 February 2020 · Accepted: 30 May 2020 ·
Published Online: 15 June 2020

Karla B. Wagner,[1] Amirreza Keyhani,[2] Andrew K. Boddorff,[1] Gregory Kennedy,[1] Didier Montaigne,[3] Brian J. Jensen,[4] Matthew Beason,[4] Min Zhou,[1,2] and Naresh N. Thadhani[1,a)]

AFFILIATIONS

[1]School of Materials Science and Engineering, Georgia Institute of Technology, Atlanta, Georgia 30332-0245, USA
[2]The George W. Woodruff School of Mechanical Engineering, Georgia Institute of Technology, Atlanta, Georgia 30332-0405, USA
[3]High Explosive Research and Development, Eglin Air Force Research Laboratory (AFRL), Eglin AFB, Florida 32542-0000, USA
[4]Shock and Detonation Physics, Los Alamos National Lab, Los Alamos, New Mexico 87545, USA

[a)]**Author to whom correspondence should be addressed:** naresh.thadhani@mse.gatech.edu. **Tel.:** 404-894-2651. **Fax:** 404-894-9140

ABSTRACT

The performance of energetic materials subjected to dynamic loading significantly depends on their micro- and meso-scale structural morphology. The geometric versatility offered by additive manufacturing opens new pathways to tailor the performance of these materials. Additively manufactured energetic materials (AMEMs) have a wide range of structural characteristics with a hierarchy of length scales and process-inherent heterogeneities, which are hitherto difficult to precisely control. It is important to understand how these features affect AMEMs' response under dynamic/shock loading. Therefore, temporally and spatially resolved measurements of both macroscopic behavior and micro- and meso-level processes influencing macroscopic behavior are required. In this paper, we analyze the shock compression response of an AMEM simulant loaded under several impact conditions and orientations. X-ray phase contrast imaging (PCI) is used to track features across the observed shock front and determine the linear shock velocity vs particle velocity equation of state, as well as to quantify the interior deformation fields via digital image correlation (DIC) analyses. Photon Doppler velocimetry is simultaneously used to measure the particle velocities of the specimens, which are consistent with those obtained from x-ray PCI. The DIC analyses provide an assessment of the average strain fields inside the material, showing that the average axial strain depends on the loading intensity and reaches as high as 0.23 for impact velocities up to 1.5 km/s. The overall results demonstrate the utility of x-ray PCI for probing "in-material" equation of state and interior strains associated with dynamic shock compression behavior of the AMEM simulant.

I. INTRODUCTION

Additive manufacturing (AM) involves the successive building of a 3D structure, layer by layer, to achieve the final shape. The process contrasts with traditional manufacturing methods, which generally involve material removal from a built block. Additive manufacturing technologies have led to mature processes for a wide range of materials, such as metals,[1,2] polymers,[3] and energetic materials.[4,5] Various AM methods have recently been used to 3D-print energetic materials. Electrospray deposition has been shown as a viable technique to deposit thin films of thermites.[6,7] Studies with electrospray techniques have incorporated a polymer binder to impart mechanical integrity to energetic materials while maintaining significant reactivity.[8] Direct ink writing (DIW) methods have demonstrated the ability to deposit energetic materials with complex sub-millimeter features.[9–11] DIW provides an affordable, flexible way to additively produce 3D objects by extruding custom-tailored inks through a nozzle via extrusion onto a computerized translation stage under constant displacement or constant pressure.[12,13]

Ultraviolet (UV) laser light curable photopolymers are widely used in DIW. Photopolymers are light sensitive monomers that cross-link and solidify when exposed to light of specific wavelengths. Photopolymers provide lower viscosity for easier printing processes and fast curing reactions, which are suitable for 3D printing of energetic materials. However, the application of 3D-printed photopolymers is limited to secondary structural parts due to their poor mechanical behavior.[14,15] DIW is capable of printing high-solids loaded precursor materials with high viscosities as demonstrated by McClain *et al.*,[16] who printed ammonium perchlorate composites at 85% solids loading by volume with less porosity than the cast method. Additionally, the filament sizes can range from sub-micrometers to millimeters, allowing for tailored structures with fine features.[17]

A consequence of the layer-by-layer build in direct ink writing additive manufacturing is the generation of process-inherent heterogeneities that can cause mechanical properties to differ significantly in different orientations and regions, as well as between builds.[18,19] Mueller *et al.*[20] studied anisotropic detonation behavior by introducing ordered linear porosity in structured UV-cured direct-ink-written energetic materials. In addition to the anisotropy, defects are unavoidable sources of microstructural heterogeneities in AM materials and can play an important role in determining their overall behavior. O'Grady *et al.*[21] determined the importance of geometry and size of defects on the detonation front in DIW energetic materials subjected to impact loading.

X-ray phase contrast imaging (PCI) is a technique in which the detector is further from the sample (on the order of 1 m) than in traditional radiographic imaging (on the order of 100 mm), and as such both refraction and absorption of x rays are utilized to create an image. This relatively large sample-to-detector distance allows wave interference due to Fresnel diffraction to appear as further contrast in addition to the already present contrast from x-ray absorption. Gradients in the index of refraction of materials, such as those at material interfaces and the wave-front of shocked samples, create interference fringes, which then highlight the interfaces. Synchrotron radiation is uniquely suited to PCI due to its high degree of beam coherence and high flux.[22–26] By combining x-ray PCI with precise timing, it is possible to probe the interior of a material during and following an impact event. This can reveal phenomena that otherwise may not be observable directly. Traditionally, such phenomena have been indirectly studied or inferred from exterior measurements or post-mortem analysis of microstructures. Thus, x-ray PCI can give an unprecedented level of detail due to its high temporal (ns) and spatial (μm) resolutions. Recently, x-ray phase contrast imaging has been used to study time- and space-resolved responses of porous periodic metal lattices, granular materials, and energetic (composite) materials during dynamic compression.[27–30]

In this paper, we analyze the shock compression response of an additively manufactured energetic material (AMEM) simulant along various loading directions with respect to the printing pattern, using high-speed x-ray PCI.[28] We take advantage of the observable features associated with the shock wave-front, and those behind it, to determine the shock velocity (U_s) and particle velocity (U_p) and obtain the equation of state. Photon Doppler velocimetry (PDV) is used to concurrently measure the AMEM sample's back surface velocity in order to help validate the equation of state developed from phase contrast images. Similarly, tracking the randomly distributed fine features and correlating their movement between successive frames offers a rare and new opportunity to obtain strain fields in the interior of the opaque samples, via digital image correlation (DIC) analysis. DIC is an optical method that takes advantage of relative changes in a sequence of images.[31] This method has been used previously in conjunction with high-speed visible light imaging,[32,33] x-ray imaging,[34] or x-ray PCI[35] to quantify the deformation fields during dynamic and impact tests. Here, we further extend the application of DIC with X-PCI to map the interior strain fields in an opaque 3D-printed material under shock loading. Overall, this paper analyzes the dynamic behavior of the heterogeneous additively manufactured energetic material simulant and demonstrates the effectiveness of x-ray phase contrast imaging in quantifying the equation of state (validated with PDV) and in combination with digital image correlation quantifying the interior strains in opaque heterogeneous materials.

II. EXPERIMENTAL PROCEDURE

A. Fabrication of AMEM simulant and sample preparation

The additively manufactured energetic material (AMEM) simulant blocks were fabricated using direct ink writing (DIW) at the Air Force Research Laboratory, Eglin Air Force Base. The ink contained ~74% by volume solid particulate with the remainder being a UV-initiated methacrylate binder (26% by volume) that results in a particulate-reinforced polymeric composite upon curing. The solid particles are comprised of four distinct populations, two organic and two inorganic in nature, with average diameters in the range of 30–100 μm. The morphologies of the particles vary from smooth spheres to jagged, rough prisms. The ink was extruded through a 1.6 mm diameter nozzle with a layer height of 1.5 mm. Figure 1(a) depicts a micro-computed tomography (μCT) image of the AMEM simulant sample showing the inorganic particles in a matrix of the binder containing organic particles. Figure 1(b) shows a scanning electron microscopy (SEM) image of the AMEM, revealing the dispersion of the organic and inorganic particles. Figure 2(a) illustrates a picture of the AM block and Fig. 2(b) shows its mesoscale structure revealing the randomly distributed inter-layer voids of differing aspect ratios. Figures 2(c) and 2(d) illustrate the 3D reconstruction of the voids and their aspect ratios relative to the respective orientation in a $20 \times 35 \times 35$ mm^3 block.

The samples ($2 \times 3 \times 6$ mm) for impact experiments were sectioned from the $5 \times 4 \times 2$ cm AM fabricated block using a diamond saw (Crystal Systems Corporation Model CU-02) at 50 RPM, controlled with a goniometer to allow accurate cuts along desired orientations. The samples were cut far from the edges of the fabricated block to avoid edge effects. A linear translation stage on the diamond saw was used to ensure that the impact faces were flat and parallel. The densities and dimensions of each sample were measured, and their orientations relative to the DIW print, and build directions were noted prior to mounting them in 9 mm diameter molds and encasing them in evacuated epoxy consisting of 70% by weight Epon-828 Resin (Miller-Stephenson Chemical Company) and 30% by weight Jeffamine T-403 hardener (Huntsman Corporation). The epoxy was cured at 70 °C for 3 h. Figures 3(a)–3(c) depict the

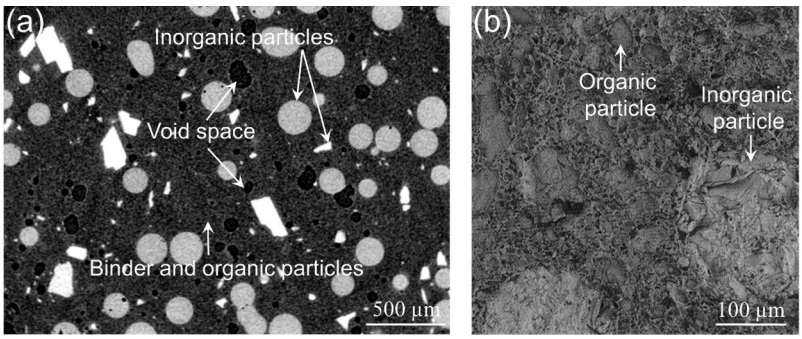

FIG. 1. (a) Micro-CT scan of the polymer–particle composite fabricated by DIW AM, showing spherical and irregularly shaped inorganic particles in a polymer binder containing a dispersion of smaller solid organic particles and (b) SEM image of the microstructure of the polymer–particle composite, showing the solid organic particles dispersed in the polymer binder surrounding the inorganic particles.

schematics of samples along different orientations relative to the print pattern. Miller indices are used to indicate the sample orientations, with red arrows pointing to the impact (loading) directions, and x and y axes, respectively, denoting the horizontal and vertical directions constituting the field of view of the PCI images obtained from impact experiments described next.

B. Plate impact experimental setup

The plate impact experiments were performed using the interchangeable powder/gas gun at the Dynamic Compression Sector at the Advanced Photon Source. Figure 4 shows a schematic of the configuration used for performing the plate impact experiments. The impact velocities ranged from 0.7 to 2.5 km/s. Solid Al 6061 impactors were used for the majority of experiments. A few experiments were performed using oxygen-free high thermal conductivity (OHFC) Cu impactors mounted on a Lexan sabot for spall studies. As shown in the schematic in Fig. 4(a), the sample assembly [Fig. 4(b)] consists of the AMEM simulant sample potted in EPON 828 epoxy, as described in Sec. II A. The assembly was machined to a 6 mm diameter cylinder and mounted in a standardized Al holder [Fig. 4(c)], with the impact face flush with its surface. Lead zirconate titanate (PZT) (Dynasen Inc.) pins were mounted, appropriately displaced from the surface, to determine the correct timing for impact velocity measurements. A single PDV probe with a 2 mm beam diameter, collimated with a working distance of 20 mm and a 1.8 mm OD lens (both collimator and probe from AC Photonics), was incorporated in the Al holder to allow measurement of the rear surface velocity, as shown in Fig. 4(c). In each experiment, the Al sample holder was attached to a standard brass ring, and then mounted onto the gun, using screws. A slit in the brass holding ring allowed the x-ray beam to travel through the sample in the appropriate orientation.

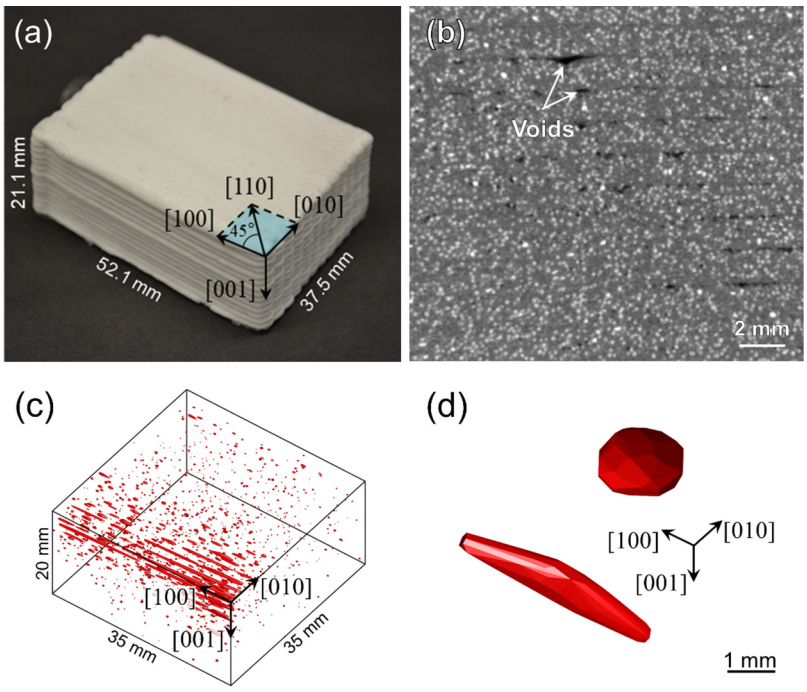

FIG. 2. (a) The as-printed material block showing orientation notations aligned along the print direction, (b) [100]–[010] cross-section of a part of the AMEM simulant block showing the presence of horizontally aligned voids, (c) 3D reconstruction of the void space obtained from micro-CT images, and (d) common void aspect ratios in the primary directions.

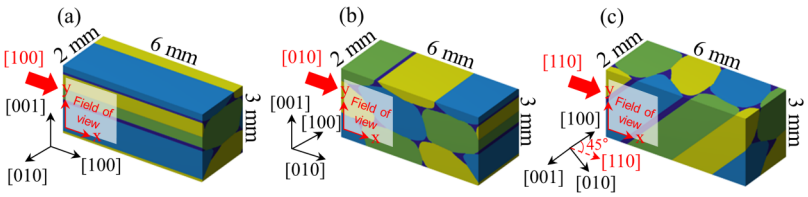

FIG. 3. Illustrations of sample orientations and impact directions with respect to AM printing pattern with each individual filament unique color: (a) loading in the x or [100] direction (filament printing direction), (b) loading in the y or [010] direction (perpendicular to the filament direction in the xy-plane), and (c) loading along the [110] direction (45° to print direction).

C. High-speed x-ray phase contrast imaging

In situ multi-frame x-ray phase contrast imaging (PCI) was performed on the samples during shock compression and spall experiments. PCI was chosen as a diagnostic tool to observe the effects of shock compression in the AMEM simulant samples, including (1) the in-material measurements of shock and particle velocities and (2) the evolution of the interior strains in the opaque heterogeneous material averaged in the direction of the x-ray beam. Synchrotron x-ray bunches from the APS arrive every 153.4 ns and transit through the EPON 828 epoxy and the AMEM sample before being detected by a lutetium oxyorthosilicate (LSO) scintillator. The x rays are converted to visible light by the scintillator and imaged by four individually gated intensified charge couple device (ICCD) PI-MAX-4 cameras (Princeton Instruments, Inc.), which are triggered to coincide with the timing of the x-ray bunches. The timing was achieved by synchronizing the ICCD triggering, the x-ray bunches, and the impact event through the use of a delay generator and two PZT timing pins. Eight images were obtained by utilizing the dual image feature of the ICCDs, allowing each camera to take two images at least 500 ns apart.[36] The inter-frame time between successive frames of the eight images is 153.4 ns, corresponding to the synchrotron x-ray bunch time. The field of view is 2.47 mm wide and ~2 mm high. Although the ICCD images are 2.5 × 2.5 mm (1024 × 1024 pixels) in size, the actual field of view on the sample is determined by the slightly smaller dimensions of the x-ray beam, which is ~2.2 × 2.2 mm (900 × 900 pixels). The samples were oriented such that the x-ray beam always traveled through the 2 mm thickness, limiting the noise in the resulting image. As shown in Fig. 3, the impact direction was along the 6 mm length of the sample (2 mm for spall experiments).

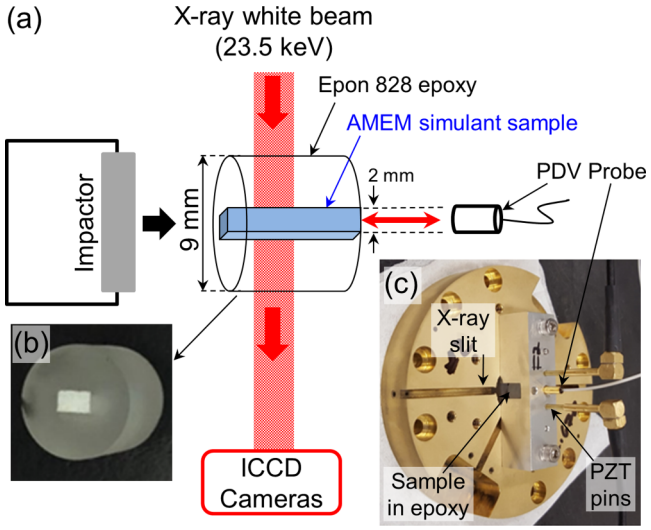

FIG. 4. Configuration of the impact experiment employing non-contact diagnostics: (a) overall layout with solid Al 6061 impactor, AMEM sample assembly, PCI arrangement (x-ray beam width illustrates field of view), and PDV probe; (b) AMEM assembly with sample potted in EPON 828 epoxy; and (c) standard Al block with sample assembly, PZT pins and connectors, and PDV probe and optical fiber mounted to a brass ring.

III. RESULTS AND DISCUSSION

Impact experiments on the AMEM simulant samples were performed at different velocities, with shock propagation along different print directions. Table I summarizes the experimental conditions and the measured parameters, including the shock rise time and shock and particle velocities obtained from x-ray PCI images. The particle velocity obtained from PDV measurements is also included in the table, to correlate with that obtained from PCI images. The majority of the experiments were performed in order to obtain equation of state data with solid Al 6061 impactors. Three experiments were performed to create spall conditions in the 2.0 mm thick AMEM samples with 1.5 mm oxygen-free high thermal conductivity (OFHC) Cu impactors mounted on Lexan sabots. X-ray PCI revealed clear contrast associated with the location of the shock front in the impacted samples. For the three spall experiments, the images showed no visible signs of spall failure, consistent with the lack of a pullback signal in the rear surface velocity profiles recorded by the PDV probes. The lack of spall is likely due to rubblization of the sample during initial shock compression, causing the material to lose tensile strength, resulting in the lack of a pullback signal. This behavior is consistent with the low static compressive strength of 20–35 MPa measured for AMEM samples.

The results and discussions presented below focus on the analysis of the x-ray phase contrast images obtained from each experiment. The shock velocity determined through the identification of the shock front and the particle velocity measured from displacement of particles immediately behind the front as observed on the images are used to generate the equation of state. Likewise, digital image correlation (DIC) analysis performed on the phase contrast images is used to obtain the interior strain fields (averaged in the direction parallel to the x-ray beam) associated with the shock compression. The Appendix describes the DIC algorithm used and the error analysis performed with the determination of the various parameters obtained from the images.

TABLE I. Summary of experimental conditions and measured parameters for the AMEM simulant analyzed, ±1 standard deviation.

Shot designation	Density (g/cm^3)	Impact direction	Impact velocity (m/s)	Shock thickness —PCI (μm)	Rise time—PCI (ns)	Shock velocity—PCI (m/s)	Particle velocity —PCI (m/s)	Particle velocity —PDV (m/s)
19-1-007	1.45	[110]	1218	34 ± 10	9 ± 2.6	3938 ± 114	855 ± 62	661 ± 48
19-1-008	1.41	[100]	1205	44 ± 6.4	11 ± 1.6	3899 ± 30	819 ± 87	726 ± 27
19-1-009	1.39	[110]	1779	37 ± 8.4	8 ± 1.8	4548 ± 47	1179 ± 92	1030 ± 39
19-1-010	1.35	[010]	1221	34 ± 8.5	9 ± 2.2	3938 ± 72	821 ± 93	730 ± 26
19-1-011	1.48	[010]	1522	45 ± 11.9	10 ± 2.7	4343 ± 82	1007 ± 138	947 ± 49
19-1-012	1.47	[100]	1517	38 ± 5.7	10 ± 1.4	3964 ± 40	1045 ± 96	871 ± 44
19-1-013	1.42	[010]	913	39 ± 10.6	11 ± 2.9	3600 ± 105	664 ± 70	480 ± 25
19-1-014	1.52	[100]	948	45 ± 11.5	12 ± 3.2	3624 ± 65	695 ± 60	522 ± 24
19-1-015	1.46	[110]	1209	46 ± 11.0	12 ± 2.8	3925 ± 86	810 ± 130	682 ± 34
19-1-016	1.50	[100]	1570	40 ± 12.9	9 ± 3.0	4320 ± 34	1040 ± 124	930 ± 38
19-1-017	1.51	[001]	1859	35 ± 11.5	7 ± 2.4	4708 ± 79	1247 ± 95	1391 ± 119
19-1-018[a]	1.58	[001]	1234	41 ± 7.5	10 ± 1.8	4171 ± 48	1208 ± 242	1027 ± 29
19-1-019[a]	1.47	[100]	2532	…	…	…	…	…
19-1-020	1.46	[010]	1762	37 ± 10	8 ± 2.3	4425 ± 24	1015 ± 129	996 ± 61
19-1-021	1.53	[110]	1827	38 ± 16.5	9 ± 3.7	4457 ± 18	1150 ± 254	969 ± 72
19-1-022[a]	1.54	[001]	1416	…	…	…	…	1122 ± 26
19-2-029	1.39	[100]	706	26 ± 8.9	8 ± 2.6	3346 ± 68	470 ± 69	437 ± 14
19-2-030	1.50	[110]	698	39 ± 9.7	12 ± 2.9	3290 ± 62	532 ± 36	337 ± 14
19-2-031	1.71	[110]	704	–	–	3307 ± 46	510 ± 83	336 ± 9

[a]Oxygen-free high conductivity Cu flyers; otherwise, Al 6061 solid impactors.

A. Equation of state

The equation of state describing the high-pressure shock compression response of the samples was determined based on measurements of the respective shock and particle velocities obtained using time-resolved phase contrast imaging diagnostics. Figure 5 shows the PCI images for a sample impacted from the left at ~900 m/s with an aluminum 6061 impactor. Loading is along the [001] direction (which corresponds to the build direction) of the AM block. It should be noted that while the phase contrast images are the aggregation of a 3D event onto a 2D plane over a 2 mm sample thickness, the measured shock and particle velocities represent averaged values through the thickness, in the interior of the material. These are unlike the volume-averaged surface measurements typically obtained with interferometry or other stress gauge-based measurements.

The propagation of the shock front and locations of distinctive particles behind the shock front were measured on successive frames. The inter-frame time of 153.4 ns was then used with the displacement measured between images to calculate the shock (U_s) and particle (U_p) velocities for the equation of state. Three measurements of each quantity were taken on each frame. The displacement measurements of the shock front were taken at the same vertical positions (top, middle, and bottom) on the front in each frame. The shock wave rise time value was obtained similarly by measuring the physical width of the front in each frame (again, three measurements were taken per frame) and dividing the width by the shock velocity in that sample. The three particle displacement measurements were obtained by tracking the three horizontally unique vertices of the smallest possible circle that surrounded each particle. Since the particle displacement was measured behind the wave-front, it was assumed that the particles underwent no additional deformation. Care was taken to identify the same features for measurement as they translated through the field of view. The resulting $U_s - U_p$ equation of state determined following the Deming regression[37,38] performed on the data obtained from the impacted samples along all orientations was found to be $U_s = (1.9047 \pm 0.0644)U_P + (2315.4 \pm 49.4)$ and is shown in Fig. 6(a). Additionally, Fig. 6(b) shows the same $U_s - U_p$ data with separate Deming regressions for the [100] direction (filament printing direction), the [010] direction (perpendicular to filament printing direction in the xy-plane), and the [110] direction (as defined in Fig. 3). The [100] direction response can be characterized by $U_s = 1.5902U_p + 2595.4$, the [010] direction by $U_s = 2.318U_p + 2046.6$, and the [110] direction by $U_s = 1.9443U_p + 2272.8$. A limited number of experiments were performed in the [001] direction since it is perpendicular to the filament printing direction, making it functionally very similar to the [010] impact orientation. It can be seen that the $U_s - U_p$ relationships presented in Fig. 6(b) for the three directions are similar to one another, suggesting little discernable orientation dependence of the equation of state. The high R^2 values and differing trends [in Fig. 6(b)] are likely due to the limited number of data points and scatter resulting from the limited number of PCI frames rather than a true effect of anisotropic behavior. It should also be noted that on average, the shock wave-front in the experiments reported here passes through a maximum of five filament interfaces of the DIW fabricated AMEM simulant, which limits the effect that larger scale defects (such as orientation dependent interfilament voids)

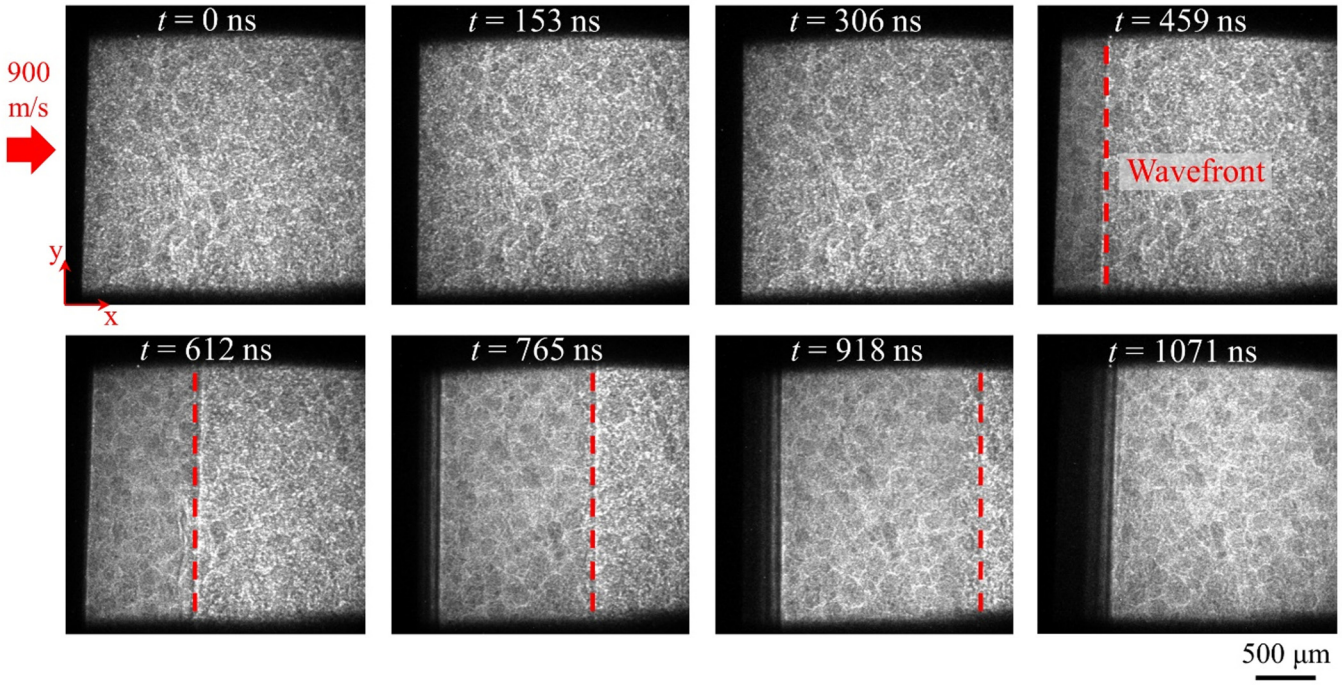

FIG. 5. X-ray phase contrast images for a sample impacted from the left at 900 m/s with an Al 6061 impactor. Loading is along the z direction (through filaments) of the AMEM.

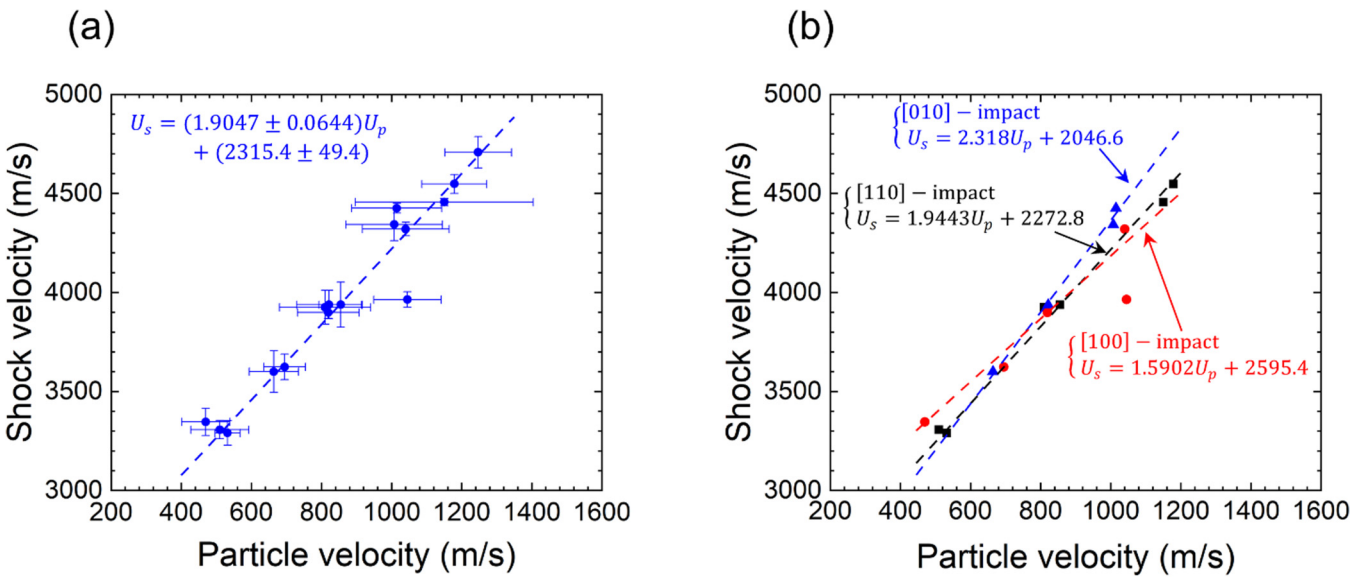

FIG. 6. Correlations by Deming regression between shock velocity and particle velocity measured by displacement tracking in PCI images: (a) overall correlation for all loading directions, with error bars as 1 standard deviation, and (b) correlations for [100], [010], and [110] directions separately, with error bars omitted for clarity.

may have on the shock compression response. The μCT images in Figs. 1 and 2 show that structural anisotropy (void content and its directional distribution) is visible in the scans only at larger length scales of the AMEM simulant block, while the smaller sample sections (dictated by the gas gun setup) used for the shock experiments have negligible voids that exhibit directionality. The porosity observed in the higher magnification images (such as seen in Fig. 1) has little directionality and does not arise from interfilament spacing. The structural observations from the μCT scans support the experimental observation of the lack of orientation dependence of the equation of state of the AMEM. Experiments performed on larger scale samples, such as on the scale of the entire AM block from which the samples were sectioned, or on samples with directionality at a smaller length scale may yet show an orientation dependence in the $U_s - U_p$ relationship.

While the determination of the shock front position and the particle displacements behind the front is relatively straightforward, the accuracy is limited by the number of frames available with a clearly visible shock front. In the present work, a minimum of two frames (at high velocities) and a maximum of four frames (at low velocities) captured the shock front positions. Furthermore, the PCI images provide a 2D projection of a 3D event, which further

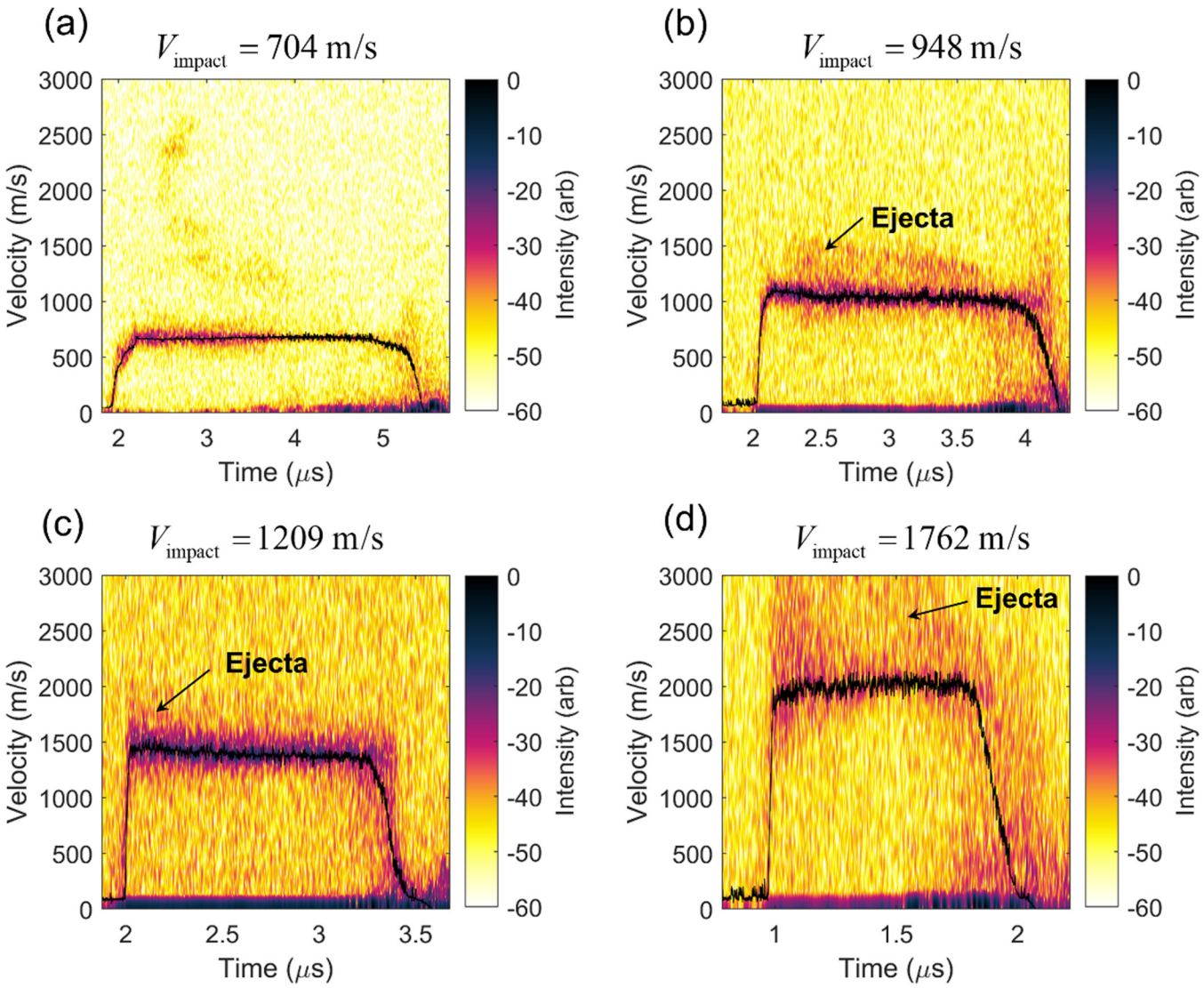

FIG. 7. PDV spectrograms showing the velocity history of the back surface of samples impacted at four different velocities: (a) 704 m/s, (b) 948 m/s, (c) 1209 m/s, and (d) 1762 m/s.

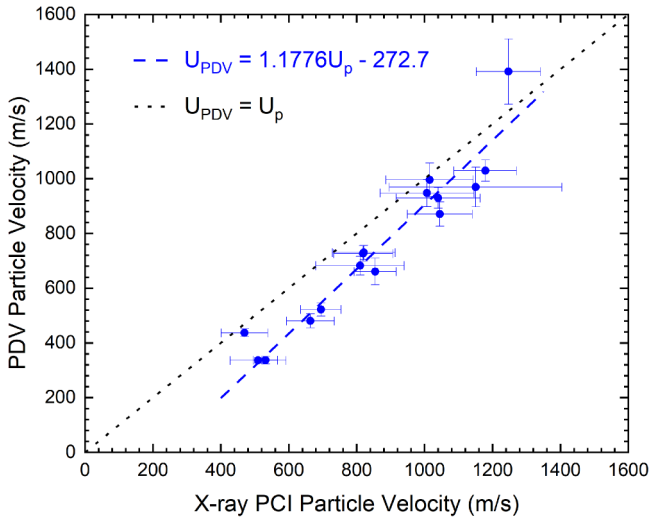

FIG. 8. Deming linear correlation between particle velocities measured by PDV (determined considering 50% of free surface velocity) and by displacement tracing on PCI images, with the parity line included for comparison.

introduces uncertainty in determining the particle velocity. These effects contribute to the data scatter in Fig. 6. Nevertheless, the use of PCI provides a valuable approach for in-material determination of the $U_s - U_p$ relation for the AMEM.

B. Photon Doppler velocimetry (PDV) for measurement of free surface motion

Free surface velocity spectrograms were generated via discrete Fourier transform (DFT) analysis[39] with a Hamming window function and global normalization. The analysis duration is 1.1 ns. Figure 7 shows examples of the PDV traces, determined via Sandia InfraRed HEtrodyne aNalysis (SIRHEN)[40] at four different impact velocities. Traces were calculated for each experiment using the robust peak finding method.[41] Figure 7 presents four representative spectrograms, ranging from low to high impact velocities, with velocity traces overlaid in black. Each trace shows an initial increase in velocity over ~100 ns, characteristic of a dispersed shock wave propagating through a rubblized material, monitored at the back of the 6-mm long sample. These rise times are approximately one order of magnitude longer than the values obtained from PCI measurements. We believe that the difference is in part due to wave dispersion and the fact that the free surface was not confined, which may cause the low and high impedance constituents to separate. In contrast, the wave fronts observed via PCI are closer to the impact surface, and, therefore, experience less dispersion as they are still in the confined interior of the sample. For the two lower velocity experiments (at 704 and 948 m/s), a knee forms before a steady velocity is achieved. The knee likely results from the viscoelasticity of the polymer[42] and the dissimilar properties of the multiple constituents present in the AMEM simulant.[43] At higher velocities, the knee cannot be identified, perhaps in part due to the stiffer behavior of the polymer at higher rates and the greater scatter seen in the PDV traces. Furthermore, most high velocity traces (as seen in Fig. 7) show evidence of an ejecta cloud whose velocities gradually decrease and approach the overall steady-state velocity.[42,44] Given the relatively low static compressive strength of the material (20–35 MPa), failure during compression followed by ejection of low impedance fragments, such as the organic binder and solids, seems plausible. The flattop displayed in the PDV spectrograms may then be arising from the more reflective and higher impedance inorganic solids. Additionally, as mentioned previously, the PDV traces for the planned spall experiments showed no evidence of a pullback signal, consistent with what would be expected of a previously rubblized material that exhibits negligible tensile strength.

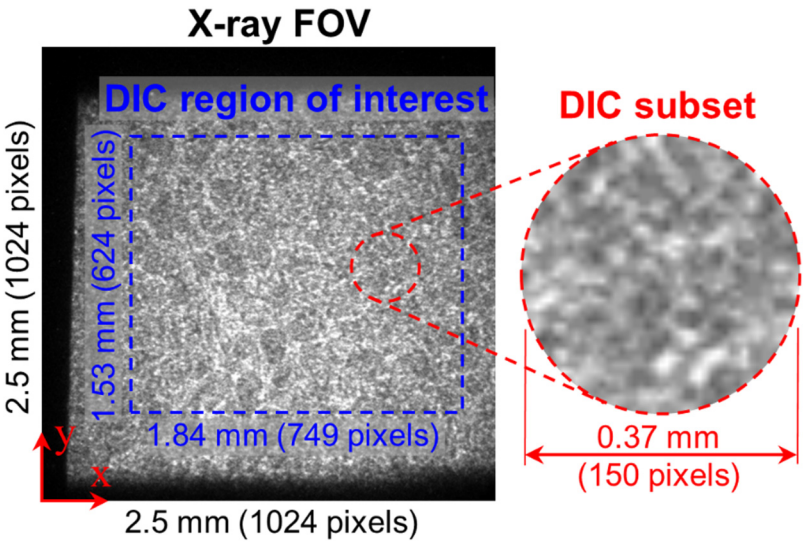

FIG. 9. An x-ray PCI image, DIC region of interest (ROI), and the DIC subset.

Based on the assumption that the free surface velocity obtained from PDV measurements is twice the particle velocity in the interior of the sample, the steady-state free surface velocity was used to calculate the particle velocity. The result is plotted against the particle velocity obtained from the x-ray phase contrast images in Fig. 8. The data in Fig. 8 are listed in the last two columns of Table I. The Deming linear regression performed on the data shows a slope close to unity (the parity line is included in Fig. 8 for comparison), suggesting overall good agreement between the two methods of particle velocity measurements. The correlation offers a rare but insightful view, enabled by the simultaneous use of the PDV and x-ray PCI diagnostics. Specifically, the velocities determined by PDV measurement (vertical axis, measured at the end of the overall 6 mm length of the impacted sample) are typically lower than the velocities determined by PCI (horizontal axis, measured within the first 2 mm of the sample). This is due to the rubblized material behind the shockwave being confined by the solid material in front of it (as in the PCI measurements), resulting in a particle velocity that is an average between those of the low and high impedance constituents. The PDV measurements, taken from the free surface of the 6 mm sample, are representative of the lower velocity and higher impedance of materials such as the solid particles. This is because the velocities measured are taken from the flattop of the spectrogram rather than the ejecta spray, which tend to be associated with the higher velocity and lower impedance of the polymer matrix.

C. Strain distributions

Time-resolved x-ray PCI of shock-compressed samples offers quantitative aggregated information about the deformation in the interior of opaque materials. Such information is generally lacking, owing to the inability to "see" inside a material. In addition to the determination of the equation of state (as described above), PCI is also used here in conjunction with the digital image correlation (DIC) technique to quantify "in-material" strains.

The DIC analysis was carried out with the Ncorr package, an open-source subset-based package with enhanced algorithms.[45] The Appendix provides a brief description of the Ncorr algorithm. Variations in the index of refraction of the material constituents spawn natural patterns in the x-ray PCI images of the samples. Proper selection of the subset size relative to the characteristic length scale of the physical features is important in DIC analyses. A subset needs to be large enough to track an arrangement of speckles/features in order to obtain correlation. To compensate for the lack of a speckle pattern here and because of the relatively large strain increment between successive frames (due to the small number of frames available), the subset needs to be large enough to obtain image correlation. A large circular subset with a diameter of 0.37 mm (150 pixels) was used (see Fig. 9). Smaller subsets than this size yield incomplete and noisy strain fields.

Figure 10 shows the evolution of the longitudinal Lagrangian strain (ε_{xx}) field. The sample is impacted by an Al 6061 impactor at ~0.9 km/s along the [010] direction. It can be seen that the strain field is rather uniform in the lateral (y) direction, and there is a gradual rise in strain along the impact direction, which is attributed to the use of a large subset size. Figure 11 shows the variations of the longitudinal strain (ε_{xx}), the lateral strain (ε_{yy}), and the shear strain (ε_{xy}) along the impact direction at the four times depicted in Fig. 10. Figure 11(a) compares the sequence of longitudinal Lagrangian strain (ε_{xx}) profiles, showing the longitudinal

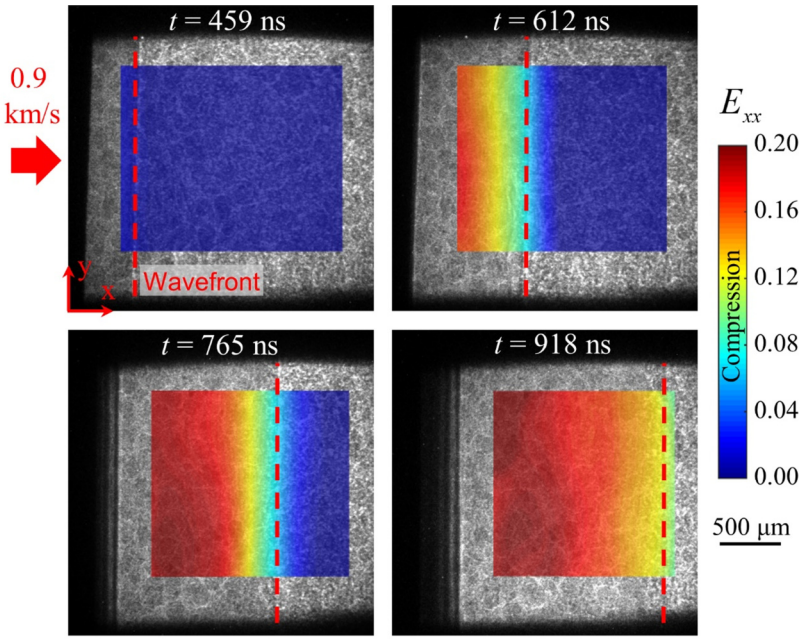

FIG. 10. Distributions of the longitudinal Lagrangian strain in a sample impacted along the [010] direction by a 6061 Al impactor at 0.9 km/s.

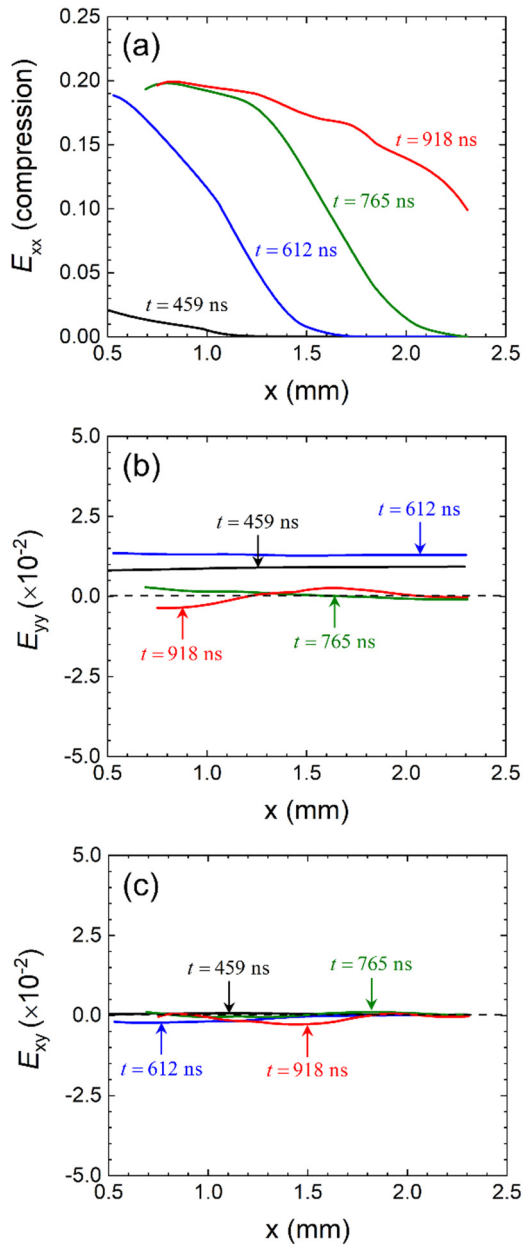

FIG. 11. Variations of the strains along the loading direction in a sample impacted along the [010] direction [Fig. 3(b)] by a 6061 Al impactor at 0.9 km/s: (a) ε_{xx}, (b) ε_{yy}, and (c) ε_{xy}.

strain level reaching a maximum of ∼0.2 and remaining at this plateau level as the wave propagates. Figures 11(b) and 11(c) show the variations of ε_{yy} and ε_{xy}, respectively. Both have magnitudes below 0.02, which is primarily within experimental error arising from the 3D nature of the deformation, since at the overall sample size scale, these strain components should average out to zero for the uniaxial strain conditions of the experiment. The macroscopically uniaxial strain conditions of planar plate impact loading of a cylindrical sample involve primary motion of material points in the direction of impact. Material heterogeneities and microstructure cause 3D interior particle motion; however, the lateral displacements in the y direction (vertical) and the z direction (normal to the image plane which is also the direction of the x-ray beam) as shown in Fig. 3 are relatively small compared with the displacement in the impact direction (x direction). Also, since the heterogeneities are random, the lateral displacements fluctuate without clear preferred direction over significant size and time scales.

Figure 12 compares the profiles of the longitudinal strain at the same time ($\sim t = 765$ ns) for two sets of samples, one set impacted along the [100] direction and the other set impacted along [010]. Each set has three samples, impacted at velocities of 0.9, 1.2, and 1.5 km/s, respectively. Both loading directions exhibit similar behaviors, while the plateau strain level increases with impact velocity. The wave-front widths obtained from DIC depend on the subset size. A larger subset leads to a wider wave-front since DIC smooths out localized deformations over the subset size; hence, the wave-front widths calculated via the x-ray PCI measurements were used. The results are shown in Fig. 12 with dotted lines. To validate the strain levels obtained from the DIC analysis, the strains were also calculated from the shock and particle velocity equation of state. Figure 13 compares the strain levels calculated using the above-mentioned techniques, showing overall good agreement in the approximate magnitudes (within error bar ranges indicated), thereby validating and providing credence to the novel use of DIC on the x-ray PCI images.

It should be noted that the use and associated interpretation of DIC performed in the present work are somewhat different from the application of DIC with images of evolving surface speckle patterns. The DIC images used here are 2D patterns resulting from the aggregated rendering of 3D interactions between x rays and the material's microstructure. As a result, the strain fields obtained are only approximate and average; they do not represent the deformation fields in any plane or 2D cross-section. As such, the fields so obtained do not sufficiently resolve fine local features of local strains such as shear bands. However, it is important to recognize that the evolution of the PCI image patterns indeed results from the deformation of the material and, therefore, reflects the strain. Hence, estimation of the overall strain levels, especially in the axial or impact direction, which is the primary direction of specimen particle motion, is possible. It should also be noted that the subset size of the images used here is relatively large (∼370 μm); consequently, the focus is on the overall trend and level, rather than local details (e.g., at the shock front). Indeed, we have refrained from making any assessment of the strains around the shock front where gradients are high in the DIC analyses.

The strain fields obtained from the DIC analyses of the x-ray phase contrast images provide insights into the interior shock response of a heterogeneous material (AMEM simulant). While the technique is quite useful, it only provides an average view of the overall strain variations and not the details of local strain distribution, owing to the fact that phase contrast images are 2D aggregate representations of heterogeneous 3D deformations. As such, averaging

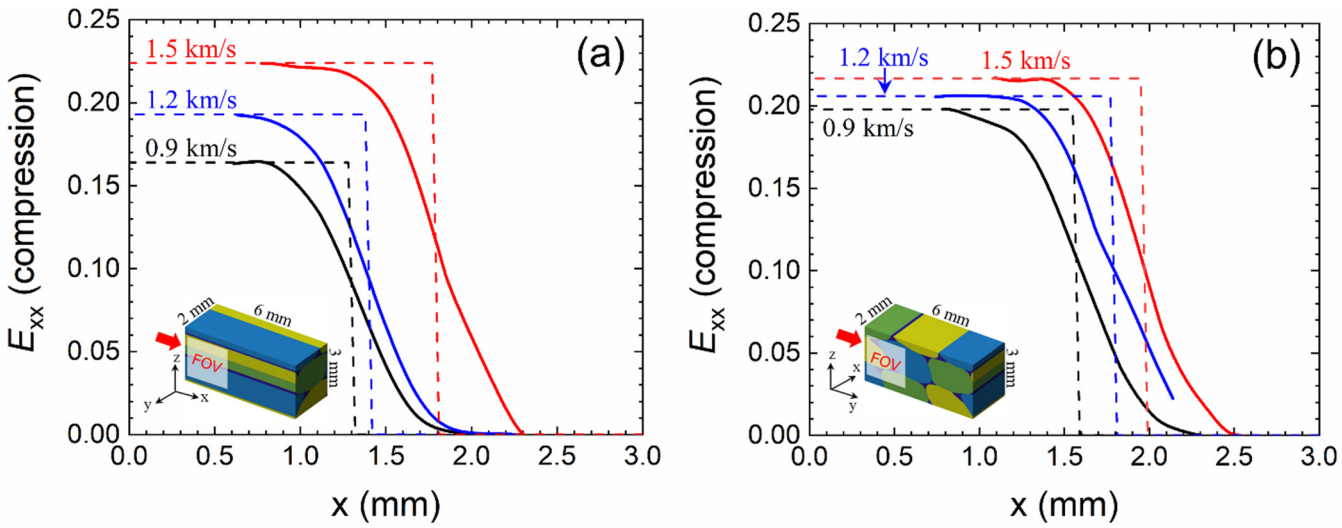

FIG. 12. Variations of the longitudinal Lagrangian strain at $\sim t = 765$ ns for samples impacted at different velocities between 0.9–1.5 km/s: (a) loading along the [100] direction and (b) loading along the [010] direction. The dotted lines show the wave-front profiles according to x-ray PCI measurements.

over a significantly large area around each image location is necessary. The subset size used here is $\sim 370\,\mu$m. The analysis is also made possible by the overall macroscopic uniaxial strain nature of the shock compression experiment. Microstructural features such as in composite systems with particles sizes of the order of $100\,\mu$m, or larger, can also function as a speckle pattern in regular DIC analyses.

Future x-ray phase contrast imaging studies are planned to investigate the shock response of AMEM simulants having more defined and anisotropic defects intentionally introduced via fabrication to reveal fundamental mechanisms as well as relations between material response and print structure, orientation, and defects.

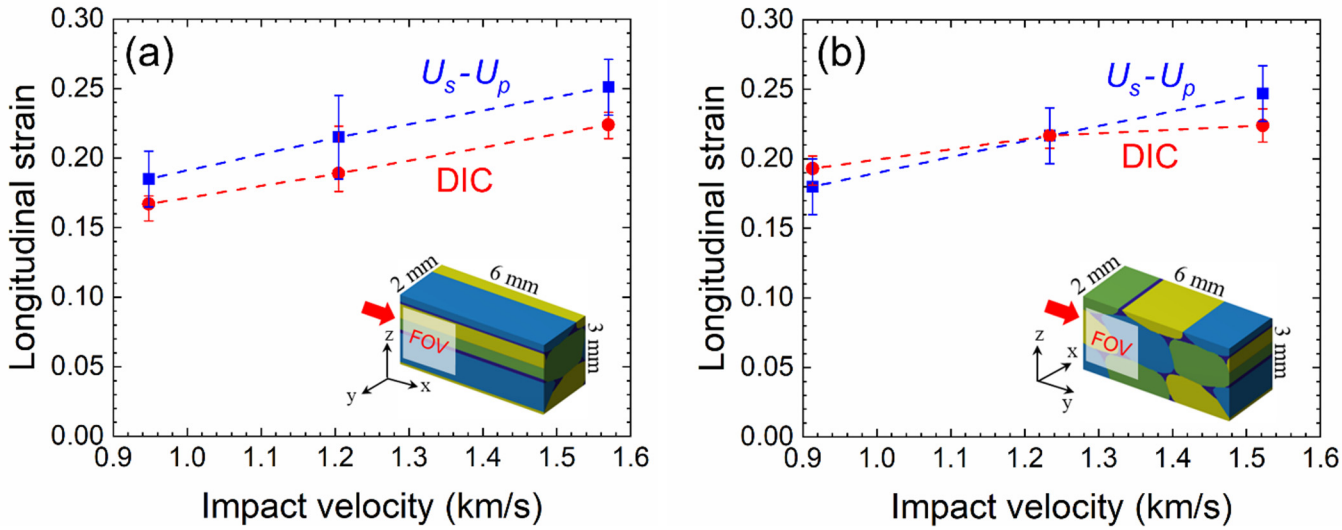

FIG. 13. Comparison of shock strain levels determined from $U_s - U_p$ measurements (blue) and via DIC analyses (red): (a) loading along the [100] direction and (b) loading along the [010] direction.

IV. CONCLUSION

The response to shock loading of an additively manufactured energetic material simulant along three directions relative to the print pattern is experimentally investigated. The samples were sectioned from a larger as-printed block. Time-resolved x-ray phase contrast imaging (PCI) was used as an interior in-material diagnostic and PDV was used as a non-contact surface diagnostic in order to validate the x-ray PCI results. The PCI with ~154 ns time resolution and 2.45 μm spatial resolution enabled the determination of shock and particle velocities from the material interior and the corresponding linear equation of state. The volume-averaged particle velocity was also obtained from surface motion captured by the PDV measurements, which revealed almost one-to-one correlation with the particle velocities obtained from PCI images. The shock responses along the different impact directions of the AMEM simulant samples, as measured by the equation of state, are similar to each other. This is likely due to the negligible amount of directional porosity on the overall scale of the samples used in the experiments reported here and the relatively low number of data points with high scatter due to a limited number of x-ray PCI frames. Therefore, the isotropic equation of state is more accurate for samples on this length scale. Digital image correlation (DIC) analysis was performed to determine the interior strains using the *in situ* x-ray PCI images. The calculated axial strains increase with shock intensity, with a maximum level of ~22% at an impact velocity of 1.5 km/s. Consistent with the conditions of the overall uniaxial impact, the strains in the two lateral directions are negligible. The strain levels obtained from the DIC analyses and those estimated from the $U_s - U_p$ equation of state measurements are consistent with each other, giving credence to the novel use of DIC on the PCI images. Overall, the results presented in this paper demonstrate the relatively isotropic shock response of the AMEM simulant on the scale of these samples and the usefulness of x-ray PCI in probing the "in-material" equation of state (in contrast to conventional techniques that rely on volume-averaged surface measurements) and in determining the average interior strains associated with shock compression.

AUTHORS' CONTRIBUTIONS

A.K. and K.B.W. are both first authors and have contributed equally to the work.

ACKNOWLEDGMENTS

This research was supported by DTRA (Project No. HDTRA1-18-1-0004). The experiments were conducted at the Dynamic Compression Sector (DCS), which is operated by the Washington State University under the U.S. Department of Energy (DOE) National Nuclear Security Administration (Award No. DE-NA0002442). Access to the DCS was through the Los Alamos National Laboratory's (LANL) Collaborative Access Team's (LCAT) beam time allocation. All PCI data reported were obtained using LANL's novel multi-frame x-ray phase contrast imaging (PCI) system developed on the IMPULSE (IMPact System for ULtrafast Synchrotron Experiments) capability at APS. Los Alamos National Laboratory is operated by Triad National Security, LLC, for the National Nuclear Security Administration of the U.S. Department of Energy (Contract No. 89233218CNA000001). Initial sample preparation used facilities in the laboratory of Dr. Martin Mourigal at Georgia Tech. The authors would like to thank the DCS team members for performing the gas gun experiments with x-ray PCI imaging and Joseph Rivera (LANL) for configuring the final samples.

APPENDIX: DIGITAL IMAGE CORRELATION ALGORITHM AND X-RAY PHASE CONTRAST IMAGE CORRECTIONS

Digital image correlation (DIC) analyses here are performed with the Ncorr, an open-source subset-based package with enhanced algorithms.[45,46] In general, a DIC technique uses a sequence of images of a sample subjected to loading and calculates the displacement/deformation fields in the sample based on the images. To achieve this, it is necessary to obtain a one-to-one correspondence between material points in the reference (undeformed) frame or image and the subsequent frames or images (deformed sample images). The DIC technique tracks small subsections of the reference image (i.e., subsets) and determines their respective locations in the deformed images. For each subset, displacement/strain fields are calculated through the transformation used to match the locations of the subset in the reference and current configurations (or frames). Subsets are selected such that they cover the whole region of interest. The selected subsets overlap with their neighbor subsets. To reduce computational effort, a spacing parameter is enforced. The displacements are interpolated assuming continuity. Strain fields calculated directly from displacements are noisy. To reduce noise levels in the strain fields, Ncorr uses a 2D Savitzky–Golay (SG) digital differentiator based on the principle of local least-square fitting with two-dimensional polynomials.[47] More details about the Ncorr DIC package can be found in Ref. 46.

Since the x-ray phase contrast images were recorded with four different camera units, it is necessary to correct the images for imperfect alignment and adjustment of the cameras. This step reduces error levels in displacement, velocity, and strain calculations. To correct for rotational misalignment and scale, the images from cameras 2, 3, and 4 were transformed based on a reference image from camera 1 taken before the experiments in order to minimize distortion levels between images recorded by the four cameras. The transformation matrices for the correction were determined by matching sped up robust features (SURF) and recovering the rotation angle and scale factor. First, SURF features were detected in each of the four images. The features were then matched by their descriptors between the reference image (camera 1) and the three reference images from the other three cameras. Outliers were removed before finding a transformation corresponding to the matched point pairs by utilizing the M-estimator Sample Consensus (MSAC) algorithm.[48] After the transformation was verified to appropriately correct the camera misalignments, it was applied to the *in situ* images for the particular sample from each camera before the U_s and U_p equation of state determination, or the DIC analysis, was performed.

To estimate distortion levels between static images recorded by the four cameras, DIC analysis was performed on each set of four x-ray images of the stationary and undeformed sample. The

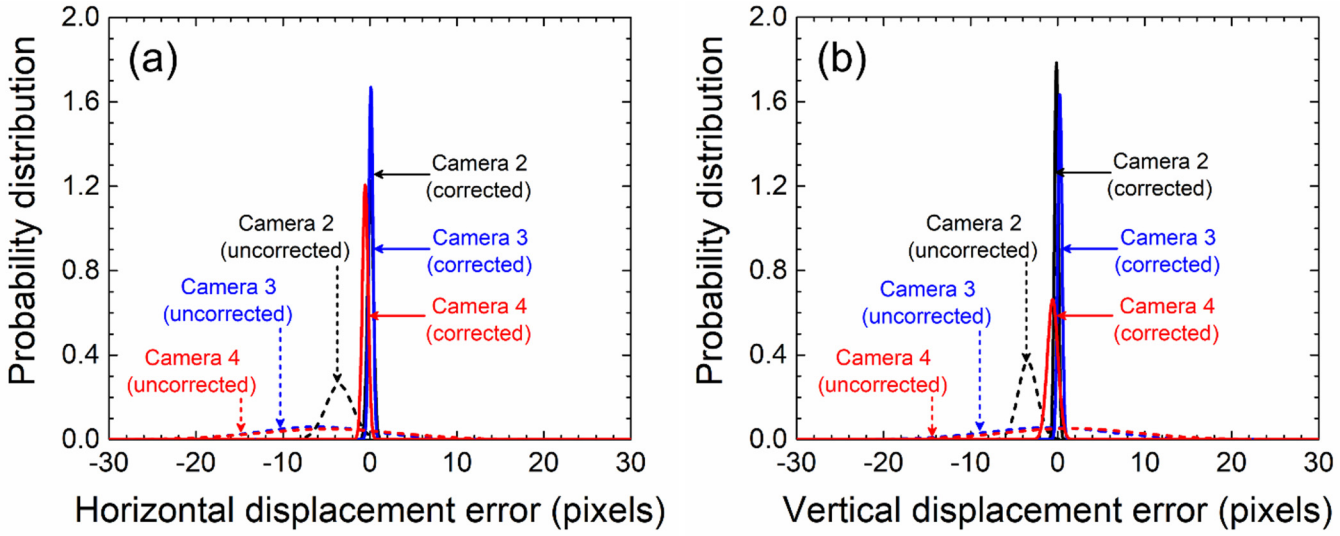

FIG. 14. Distributions of displacement errors in corrected and uncorrected images recorded by cameras 2, 3, and 4 relative to camera 1" (a) horizontal displacement error and (b) vertical displacement error.

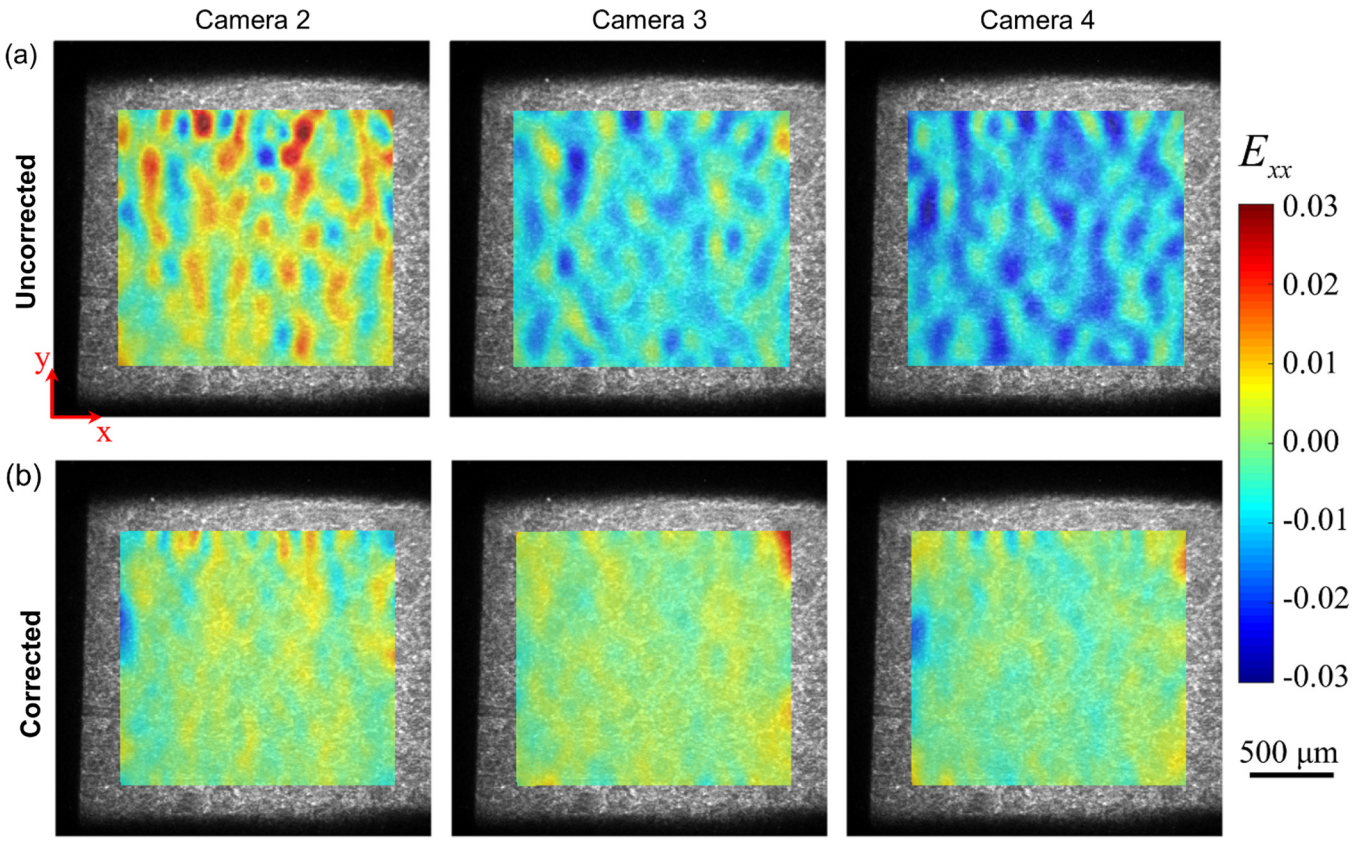

FIG. 15. (a) Longitudinal strain errors ($\Delta\varepsilon_{xx}$) in images recorded by cameras 2, 3, and 4 relative to camera 1, and (b) longitudinal strain errors in cameras 2, 3, and 4 after image corrections.

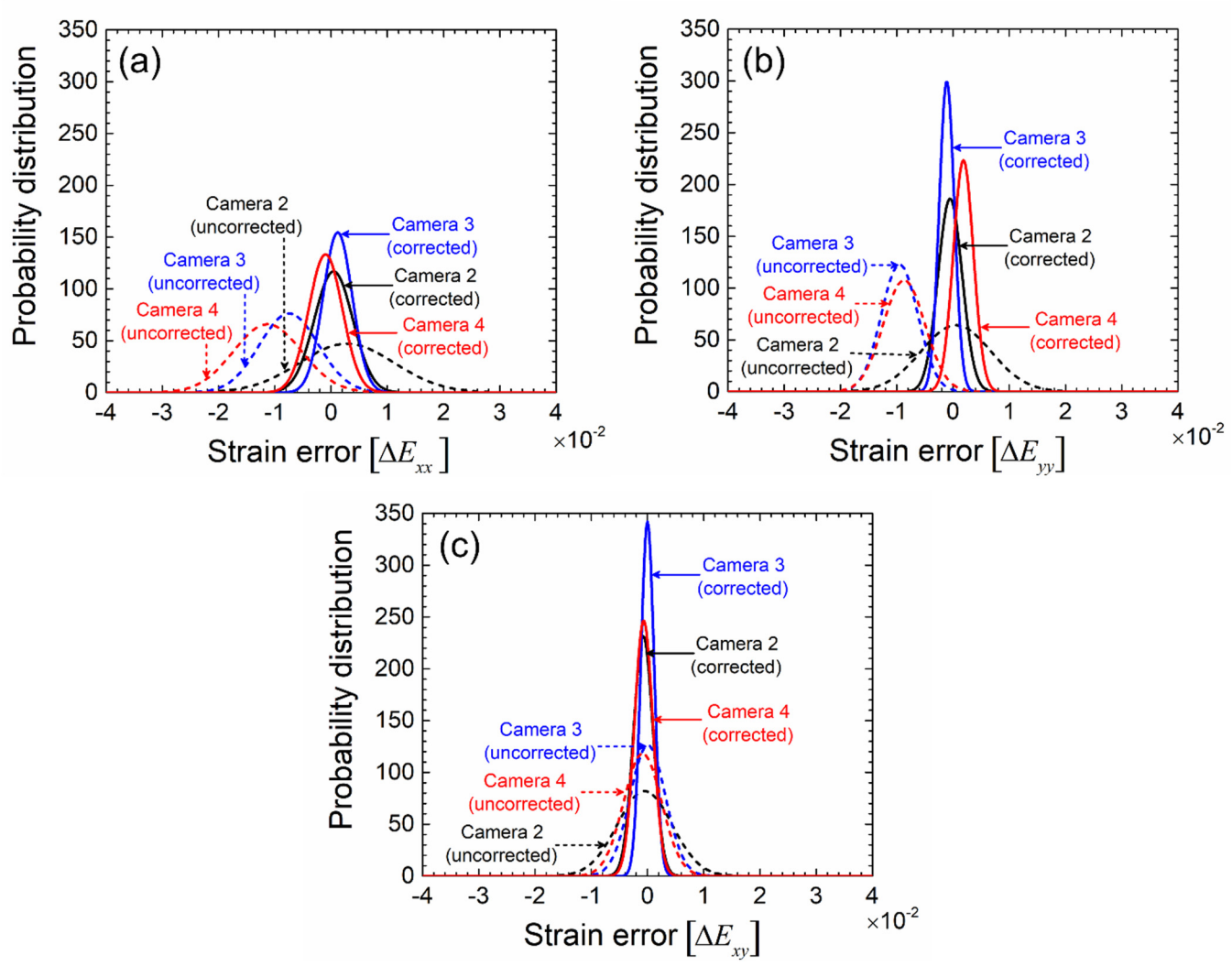

FIG. 16. Distributions of strain errors in corrected and uncorrected images recorded by cameras 2, 3, and 4 relative to camera 1: (a) axial strain error, (b) lateral strain error, and (c) shear strain error.

image recorded by camera 1 was then used as the reference frame, and relative displacement and strain fields in images from cameras 2 to 4 were independently calculated for each experiment. Ideally, these relative deformation and strain fields in images should be zero since the sample in the image was not yet subject to translation or deformation. However, as a result of the misalignments of the cameras, the DIC analysis yielded non-zero displacement and deformation fields. Figure 14 compares the horizontal and vertical displacement error distributions in corrected and uncorrected images recorded by cameras 2–4. The maximum displacement error in images recorded by cameras 2–4 is ~20 pixels. The correction reduced the error to a negligible level of ~2 pixels (~5 μm). The strain tensor used in this work is the Lagrangian strain.[49] Figure 15(a) shows the longitudinal strain (ε_{xx}) error maps for images recorded by cameras 2–4 before the correction. The maximum longitudinal strain error level in all images is ±3%. Figure 15(b) shows the corresponding error maps after the corrections were performed. The maximum error was thus reduced to under ±1%. Figure 16 shows the probability distribution of the three strain components for the corrected and uncorrected images recorded by cameras 2–4. The maximum strain error for all components is decreased from ±3% to ±1% after image correction is performed.

DATA AVAILABILITY

The data that support the findings of this study are available from the corresponding author upon reasonable request.

REFERENCES

[1]D. Herzog, V. Seyda, E. Wycisk, and C. Emmelmann, Acta Mater. **117**, 371 (2016).
[2]W. E. Frazier, J. Mater. Eng. Perform. **23**, 1917 (2014).
[3]K. V. Wong and A. Hernandez, ISRN Mech. Eng. **2012**, 1 (2012).
[4]A. K. Murray, T. Isik, V. Ortalan, I. E. Gunduz, S. F. Son, G. T.-C. Chiu, and J. F. Rhoads, J. Appl. Phys. **122**, 184901 (2017).
[5]T. J. Fleck, A. K. Murray, I. E. Gunduz, S. F. Son, G. T. C. Chiu, and J. F. Rhoads, Addit. Manuf. **17**, 176 (2017).
[6]H. Wang, J. B. DeLisio, G. Jian, W. Zhou, and M. R. Zachariah, Combust. Flame **162**, 2823 (2015).
[7]H. Wang, G. Jian, G. C. Egan, and M. R. Zachariah, Combust. Flame **161**, 2203 (2014).
[8]C. Huang, G. Jian, J. B. DeLisio, H. Wang, and M. R. Zachariah, Adv. Eng. Mater. **17**, 95 (2015).
[9]A. C. Ihnen, W. Y. Lee, B. Fuchs, A. M. Petrock, and D. Stec III, "Ink jet printing and patterning of explosive materials," U.S. patent 9,296,241 B1 (2016).
[10]F. Ruz-Nuglo, L. Groven, and J. A. Puszynski, "Additive manufacturing for energetic components and materials," in *50th AIAA/ASME/SAE/ASEE Joint Propulsion Conference 2014* (2014), Vol. 7, pp. 5865–5691.
[11]A. S. Tappan, J. P. Ball, and J. W. Colovos, "Inkjet printing of energetic materials: Sub-micron Al/MoO_3 and Al/Bi_2O_3 thermite," Sandia National Laboratories Presentation SAND2011-8957C, Sandia National Laboratory, Albuquerque, NM, 2012.
[12]D. B. Chrisey, Science **289**, 879 (2000).
[13]J. A. Lewis and G. M. Gratson, Mater. Today **7**, 32 (2004).
[14]J. W. Stansbury and M. J. Idacavage, Dent. Mater. **32**, 54 (2016).
[15]W. Oropallo and L. A. Piegl, Eng. Comput. **32**, 135 (2016).
[16]M. McClain, I. Gunduz, and S. Son, Proc. Combust. Inst. **37**, 3135 (2019).
[17]J. A. Lewis, Adv. Funct. Mater. **16**, 2193 (2006).
[18]C. Lee, S. Kim, H. Kim, and S. Ahn, J. Mater. Process. Technol. **187–188**, 627 (2007).
[19]S.-H. Ahn, M. Montero, D. Odell, S. Roundy, and P. K. Wright, Rapid Prototyping J. **8**, 248 (2002).
[20]A. Mueller, A. Schmalzer, P. Bowden, B. Tappan, A. White, and R. Menikoff, Bull. Am. Phys. Soc. **64**, 63 (2019).
[21]C. O'Grady, A. Tappan, R. Knepper, S. Rupper, J. Vasiliauskas, and M. Marquez, Bull. Am. Phys. Soc. **64**, 63 (2019).
[22]B. Jensen, S. Luo, D. Hooks, K. Fezzaa, K. Ramos, J. Yeager, K. Kwiatkowski, T. Shimada, and D. Dattelbaum, AIP Adv. **2**, 012170 (2012).
[23]B. Jensen, C. Owens, K. Ramos, J. Yeager, R. Saavedra, A. Iverson, S. Luo, K. Fezzaa, and D. Hooks, Rev. Sci. Instrum. **84**, 013904 (2013).
[24]S. C. Mayo, A. W. Stevenson, and S. W. Wilkins, Materials **5**, 937 (2012).
[25]A. Stevenson, T. Gureyev, D. Paganin, S. Wilkins, T. Weitkamp, A. Snigirev, C. Rau, I. Snigireva, H. Youn, I. Dolbnya, W. Yun, B. Lai, R. Garrett, D. Cookson, K. Hyodo, and M. Ando, Nucl. Instrum. Methods Phys. Res. B **199**, 427 (2003).
[26]S. Wilkins, T. E. Gureyev, D. Gao, A. Pogany, and A. Stevenson, Nature **384**, 335 (1996).
[27]R. Crum, M. Homel, D. Pagan, E. Herbold, D. Miller, J. Lind, B. Jensen, A. Iverson, and M. Akin, J. Appl. Phys. **125**, 025902 (2019).
[28]N. Parab, Z. Roberts, M. Harr, J. Mares, A. Casey, I. E. Gunduz, M. Hudspeth, B. Claus, T. Sun, K. Fezzaa, S. Son, and W. Chen, Appl. Phys. Lett. **109**, 131903 (2016).
[29]J. Mares, Z. Roberts, I. E. Gunduz, N. Parab, T. Sun, K. Fezzaa, W. Chen, S. Son, and J. F. Rhoads, Appl. Mater. Today **15**, 286 (2019).
[30]B. Branch, A. Ionita, B. Clements, D. Montgomery, B. Jensen, B. Patterson, A. Schmalzer, A. Mueller, and D. Dattelbaum, J. Appl. Phys. **121**, 135102 (2017).
[31]B. Pan, K. Qian, H. Xie, and A. Asundi, Meas. Sci. Technol. **20**, 062001 (2009).
[32]J. Y. Huang, Y. Li, Q. C. Liu, X. M. Zhou, L. W. Liu, C. L. Liu, M. H. Zhu, and S. N. Luo, Phys. Rev. B **92**, 144101 (2015).
[33]S. Ravindran, A. Tessema, A. Kidane, and J. Jordan, J. Appl. Phys. **125**, 145104 (2019).
[34]W. G. Proud, D. M. Williamson, J. E. Field, and S. M. Walley, Chem. Cent. J. **9**, 52 (2015).
[35]L. Lu, D. Fan, B. Bie, X. Ran, M. Qi, N. Parab, J. Sun, H. Liao, M. Hudspeth, and B. Claus, Rev. Sci. Instrum. **85**, 076101 (2014).
[36]B. J. Jensen, B. Branch, F. J. Cherne, A. Mandal, D. S. Montgomery, A. J. Iverson, and C. Carlson, "Dynamic behavior of materials," in *Conference Proceedings of the Society for Experimental Mechanics Series*, edited by J. Kimberley, L. Lamberson, and S. Mates (Springer, 2019), Vol. 1, pp. 89–93.
[37]W. E. Deming, *Statistical Adjustment of Data*, 2nd ed. (Dover Publications, New York, 1943).
[38]J. Browaeys, *Linear fit with both uncertainties in x and y*, version 1.2.0.0 (MATLAB Central File Exchange, 2017).
[39]O. T. Strand, D. R. Goosman, C. Martinez, T. L. Whitworth, and W. W. Kuhlow, Rev. Sci. Instrum. **77**, 083108 (2006).
[40]D. H. Dolan, *Sandia InfraRed HEtrodyne aNalysis*, version 1.0 (GitHub, 2016).
[41]T. Ao and D. H. Dolan, "SIRHEN: A data reduction program for photonic Doppler velocimetry measurements," Sandia National Laboratories Report SAND2010-3628, 2010.
[42]D. B. Holtkamp, in *IEEE International Conference on Megagauss Magnetic Field Generation and Related Topics*, edited by G. E. Kiuttu, P. J. Turchi, and R. E. Reinovsky (IEEE, 2006), Vol. 10703, pp. 119–128.
[43]M. B. Rauls and G. Ravichandran, in *Proceedings of the 2015 Hypervelocity Impact Symposium (Hvis 2015)* (Elsevier, 2015), Vol. 103, p. 515.
[44]A. V. Andriyash, M. V. Astashkin, V. K. Baranov, A. G. Golubinskii, D. A. Irinichev, A. N. Kondrat'ev, S. E. Kuratov, V. A. Mazanov, D. B. Rogozkin, S. N. Stepushkin, and V. Y. Khatunkin, J. Exp. Theor. Phys. **122**, 970 (2016).
[45]J. Blaber, B. Adair, and A. Antoniou, Exp. Mech. **55**, 1105 (2015).
[46]B. Pan, Appl. Opt. **48**, 1535 (2009).
[47]B. Pan, H. Xie, Z. Guo, and T. Hua, Opt. Eng. **46**, 033601 (2007).
[48]H. Bay, A. Ess, T. Tuytelaars, and L. Van Gool, Comput. Vis. Image Understanding **110**, 346 (2008).
[49]L. E. Malvern, *Introduction to the Mechanics of a Continuous Medium* (Prentice-Hall, 1969).